ASME Journal of Mechanisms and Robotics
Online journal at:
https://asmedigitalcollection.asme.org/mechanismsrobotics

Straight-Line Metamaterial Approximating an Ideal Shear Cell[1]

Luuk Schattenberg
Department of Precision and Microsystems Engineering,
Delft University of Technology,
Delft 2628 CD, The Netherlands
e-mail: lh.schattenberg@gmail.com

Pierre Roberjot[2]
Department of Precision and Microsystems Engineering,
Delft University of Technology,
Delft 2628 CD, The Netherlands
e-mail: p.roberjot@tudelft.nl

Just L. Herder
Department of Precision and Microsystems Engineering,
Delft University of Technology,
Delft 2628 CD, The Netherlands
e-mail: j.l.herder@tudelft.nl

Mechanical metamaterials are architected structures designed to exhibit unconventional mechanical responses. Their engineered properties make them especially valuable for realizing precise motion and load-bearing functions, with broad applications in machines, robotics, and related technologies. Straight-line mechanisms, typically based on compliant or rigid designs, offer compactness and accuracy but are often limited by parasitic motion, restricted range of motion, and load-capacity constraints. In this work, we introduce the concept of shear cell, develop a suitable embodiment, and demonstrate how a planar straight-line metamaterial mechanism approximates its behavior. Both series and parallel tessellations of a rectangular shear cell are investigated, considering full and partial scaling strategies. Through analytical modeling, finite element simulations, and experimental validation, we examine how tessellation influences key performance parameters, including range of motion, stiffness, and crosstalk. Finally, the concept is extended to demonstrate the design of planar multi-degrees-of-freedom mechanisms and spatial straight-line metamaterial motion systems. [DOI: 10.1115/1.4071121]

Keywords: straight line mechanism, metamaterial, shear mechanism, mechanism design

1 Introduction

Mechanical metamaterials are engineered structures designed to exhibit mechanical properties that are rare or absent in natural materials [1,2]. Examples include negative or zero Poisson's ratio [1,3,4], tunable stiffness [5], multistability [6,7], and shape memory [8]. These behaviors arise from carefully structured and tessellated unit cells, which can be tailored to achieve specific mechanical responses.

Motion systems typically consist of three fundamental components: a guiding structure, an actuator, and a sensor. Embedding metamaterials into motion systems, or designing motion systems directly from metamaterials, could enable compact architectures by integrating actuation and sensing within the guiding structure. Metamaterial mechanisms [9] aim to replicate the function of traditional motion components. To achieve this, metamaterials must be designed for specific motions such as rotation [10], twist [11], expansion [12], or compression [13]. The architected nature of these structures further offers opportunities to enhance and extend the functionality of motion systems. Straight-line motion systems, a class of compliant mechanisms, are of particular interest in this context [14].

Straight-line motion systems are mechanisms in which the end effector follows a straight path. Two categories exist: exact straight-line mechanisms, in which a coupler point traces a mathematically perfect straight line (e.g., Peaucellier–Lipkin [15,16] and Hart's inversors [17]); and approximate straight-line mechanisms, which generate a near-straight trajectory over a finite range with small deviations (e.g., Watt's [18], Roberts [19,20], and Evans [21] linkages).

Despite recent progress in straight-line motion systems [22,23], the influence of tessellation on metamaterial behavior remains insufficiently explored. In addition, the design of metamaterials for predefined machine functions—such as straight-line motion or tip-tilt—is still rare. Most prior studies focus on isolated properties rather than their combined effects. For instance, Zhang et al. [24] examined how the number of parallel unit cells affects tilted stable configurations. Another example is multistability, where increasing the number of bistable unit cells in series introduces additional stable positions [6,7]. More recently, the development of configuration-indifferent building blocks has enabled unit cells to be repositioned without altering the global degrees-of-freedom (DOF) [25]. While these approaches highlight the potential of metamaterials in motion applications, systematic methods for designing motion properties remain limited, and no guidelines currently exist for selecting the optimal number or scale of unit cells. Straight-line motion systems in particular could benefit from the development of an ideal shear metamaterial, which would eliminate parasitic motion and enable a wide range of applications.

This article introduces the design of a straight-line metamaterial motion system based on an approximation of an ideal shear unit cell. We first define approximate and ideal shear cells, then propose selection criteria for straight-line mechanisms to serve as shear cells. The Roberts linkage is chosen as an embodiment of an approximate shear cell, which is then tessellated in series and parallel to form a planar metamaterial system. We develop an analytical model and validate it with finite element simulations (FEM) and experiments to analyze the evolution of key parameters, including range of motion (ROM), crosstalk, and stiffness. Finally, extensions of the planar straight-line metamaterial toward planar multi-degrees-of-freedom and spatial straight-line metamaterial motion systems are presented.

[1]Paper presented at the ASME International Design Engineering Technical Conferences & Computers and Information in Engineering Conference (IDETC-CIE 2025), Aug. 17–20, 2025.
[2]Corresponding author.
Contributed by Mechanisms and Robotics Committee of ASME for publication in the Journal of Mechanisms and Robotics. Manuscript received August 15, 2025; final manuscript received September 30, 2025; published online February 25, 2026. Assoc. Editor: Giovanni Berselli.

2 Method

In this section, we introduce and define the concept of an approximate and ideal shear cell. The Roberts linkage is then selected as a case study to design and demonstrate a shear unit cell. This unit cell is subsequently tessellated in a planar arrangement, where the effects of scaling are examined. Finally, the analytical findings are validated through FEM and experimental testing.

2.1 Ideal Shear Cell. Metamaterial mechanisms were introduced as metamaterials that perform a pre-defined function [9] and where the building blocks tend to achieve a specific motion. A key building block in the design of metamaterial mechanisms is the shear cell, depicted in Fig. 1(*a*). It consists of a square frame with stiff edges and flexible corners that enable the rotation of the edges. The shearing motion follows a circular trajectory, as shown in Fig. 1(*a*), leading to significant crosstalk between the shearing motion and vertical displacement. At the extreme position of 90 deg, this vertical displacement even equals the horizontal displacement. Eliminating this crosstalk leads to two possible concepts. First, the use of an ideal shear cell, illustrated in Fig. 1(*b*), which enables linear motion while constraining the other degrees-of-freedom. Second, the use of an approximate shear cell tessellated in series and parallel in order to reduce or control the crosstalk. In addition to motion-based descriptions, the ideal shear cell can also be analyzed in terms of stiffness. In an ideal motion system, the desired DOF has zero stiffness whereas the other two translational and three rotational degrees-of-freedom are infinitely stiff.

A double leaf spring [26] is a common design that replicates the behavior of a shear cell. For linear motion, a folded flexure linear guide eliminates crosstalk by placing two double leaf springs in series, effectively canceling the equal and opposite crosstalk. This illustrates how tesselation can reduce or eliminate crosstalk, motivating the second approach.

Next to the well-known examples, three distinct methods were found to approximate ideal shear behavior. The first approach, compliant rolling-contact architected materials (CRAMs) [27], utilizes flexures to constrain rolling contact between rigid bodies, enabling pure shear motion when circular cams are used. By predeforming the flexures, CRAMs achieve near-zero DOF stiffness while maintaining high constraint stiffness. Another approach is straight-line mechanisms, which generate approximate or exact straight-line motion either at a single point or across an entire body, with various designs documented in the literature. For instance, the Roberts mechanisms [19,20], offer compact and simple solutions, while others, such as the Peaucellier–Lipkin mechanism [15,16], can be more complex, though their compliant counterparts are currently limited in range of motion. Finally, error compensation utilizes generalized cross-spring pivots to eliminate parasitic motion in four-bar mechanisms by carefully designing the flexures to account for center shifts [14,28]. This approach enables fully compensated designs, achieving performance comparable to exact straight-line mechanisms. Additionally, the method can be used to develop families of optimized designs [28].

2.2 Unit Cell Selection. A wide variety of straight-line mechanisms have been developed, exhibiting both approximate and exact straight-line behaviors. This section outlines the criteria and requirements for selecting a mechanism suitable for the design of planar straight-line metamaterials.

Restricting the design to a planar metamaterial excludes spatial straight-line mechanisms such as the Sarrus linkage, its inspired variants [29,30], and single- or multi-loop spatial linkages [31]. The mechanism must be strictly planar, with no overlapping parts, which rules out options such as the Chebyshev linkage, the Bricard inversor, and Watt's parallel motion linkage [22]. Furthermore, the mechanism should incorporate a fixed base and a clearly defined end effector to enable straightforward integration with neighboring unit cells. For medium- to large-scale fabrication methods, such as additive manufacturing or laser cutting, the design must also be realizable as a monolithic compliant structure. Two straight-line mechanisms satisfy these requirements: the exact Peaucellier–Lipkin inversor and the approximate Roberts linkage.

The objective of this work is to investigate how tessellation influences range of motion, crosstalk, and stiffness. The Peaucellier–Lipkin inversor, by virtue of its exact straight-line motion, exhibits no crosstalk. Consequently, this study focuses on exploring the effects of tessellation on the approximate Roberts linkage.

2.3 Unit Cell Design—Compliant Roberts Linkage. Even though CRAMs best approximate ideal shear behavior, they require assembly and complex analysis. While Roberts mechanisms are compact and possess a good range of motion, they also present crosstalk. However, their simplicity allows for swift analysis and investigation of this non-zero crosstalk. In the following, the Roberts mechanism is used as the approximate shear cell (Fig. 2) for the development of straight-line metamaterial mechanisms.

To optimize the shear cell for large ROM, leaf springs are used in the links 2 and 4 [19,20], illustrated in Fig. 2. To facilitate straightforward tessellation in the x and y directions, a C-shaped frame is added around the mechanism to ensure that the input link is positioned opposite to the base link within the unit cell. This topology enables the shear cell to be tessellated as a square or rectangular cell. The reference design [20] employs a small flexure at joint 5, suitable for small angle rotations. To obtain larger displacements, the flexure joint is replaced by a cartwheel [32], as its simple 2D extruded geometry still allows for relatively large rotation. The adapted unit cell, shown in Fig. 2, illustrates two unit cells in parallel. The Roberts mechanism is an approximate straight-line mechanism at a single point (joint 5), and by coupling two cells, the straight-line motion extends from a single point to the full output link, transitioning from path generation to motion generation [33].

The unit cell can be modeled as a pseudo-rigid body model (PRBM) [33], where the kinematics follow from the rigid links and revolute joints, while the kinetics follow from the torsional springs. The PRBM is represented in Fig. 3(*a*), with joints 1 through 4 originating from the leaf springs and joint 5 from the cartwheel. The PRBM assumes that the output link remains horizontal, causing joint 5 to rotate during displacement. When the unit cell is tessellated in parallel to form a metamaterial, this

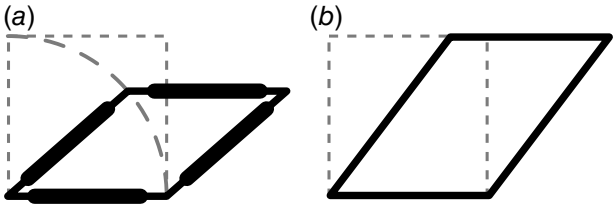

Fig. 1 Representation of (*a*) the shear cell [9] and its deformation, and (*b*) an ideal shear cell and its deformation

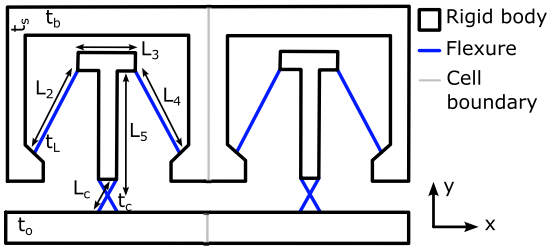

Fig. 2 Illustration of a parallel tessellation of two Roberts shear cells, showing dimensions

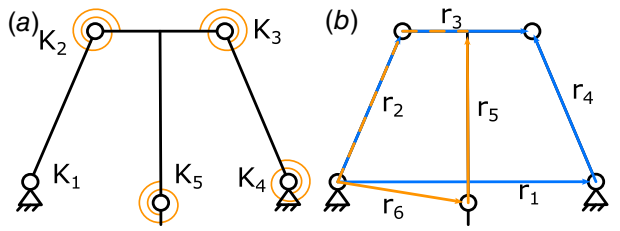

Fig. 3 Representation of (*a*) the PRBM and (*b*) the two vector loops

rotation becomes constrained. Additionally, joints 1 and 4 are rigidly connected to the base, assuming an infinitely stiff frame.

To determine the output displacement and link angles, two vector loops are used. The first vector loop (Eq. (1)) is used to derive the joint angles of the four-bar mechanism (r_1-r_2-r_3-r_4), shown in Fig. 3(*b*), while the second vector loop (Eq. (2)) calculates the output displacement (r_2-r_3-r_5-r_6), shown in Fig. 3. The angles of the links are measured from the positive x-axis to vector $\vec{r_i}$, with the vector sum evaluated in a clockwise direction.

$$\vec{r_1} + \vec{r_3} - \vec{r_4} - \vec{r_1} = \vec{0} \tag{1}$$

$$\vec{r_2} + \frac{1}{2}\vec{r_3} - \vec{r_5} - \vec{r_6} = \vec{0} \tag{2}$$

The actuation force, and consequently stiffness, are derived using virtual work and Freudenstein's kinematic coefficients [33]. For the fixed–fixed condition of the leaf springs, the torsional stiffness is written as

$$K_{1-4} = 2\gamma K_\Theta \frac{EI}{L} \tag{3}$$

with E the Young's modulus, I the area moment of inertia, L the characteristic length, stiffness coefficient $K_\Theta = 2.65$, and characteristic radius factor $\gamma = 0.8517$ [33]. The torsional stiffness for the cartwheel [32,34] is defined as

$$K_5 = \frac{8EI}{L} \tag{4}$$

The resulting force is expressed as

$$F = \frac{1}{\frac{D\delta\theta_2 + E\delta\theta_3}{A\delta\theta_2}} + \frac{1}{\frac{D\delta\theta_2 + E\delta\theta_3}{B\delta\theta_3}} + \frac{1}{\frac{D\delta\theta_2 + E\delta\theta_3}{C\delta\theta_4}} \tag{5}$$

where A, B, C, D, and E represent substituted expressions, which are provided in Appendix along with a more extensive derivation. The different divisions of $\delta\theta$ are solved using Freudenstein's kinematic coefficients. The formulas are combined in PYTHON to compute the force. Once force and displacement are determined, their ratio yields the DOF stiffness K_x.

To calculate the range of motion, the stress of the flexure is compared to the yield stress of the material. In this analysis, which focuses on relative change rather than actual application, no safety factor is applied. The stress in the leaf springs is also derived from the PRBM. For the fixed-fixed leaf spring, the stress is estimated using the equation for a fixed-guided flexure [33]. This provides an equivalent estimate of the maximum bending stress, which is sufficient for the present analysis focused on relative changes in the unit cells. The equivalent force, P, required to deform the leaf spring to angle θ is calculated, as shown in Eq. (6). Here, θ is selected as the maximum of the four angles obtained from the vector loop equations. The maximum stress in the leaf spring is then determined using Eq. (7). In this equation, $\frac{Pa}{2}$ represents the reaction moment, with the expression for a derived in Appendix, and c is the distance to the centerline of the flexure. In PYTHON, the maximum stress is computed and compared to the yield stress. Once the yield stress is exceeded, the maximum displacement is recorded.

Table 1 Dimensions of the shear cell in millimeters

Dim.	Series/Parallel	Series FT	Parallel FT	Scaling
$L_{2,4,5}$	19.8	19.8	19.8	26.64
L_3	17.25	17.25	17.25	22.2
L_c	9.6	9.6	9.6	12.58
t_L	0.61	0.48	0.76	0.81
t_c	0.49	0.39	0.62	0.66
$t_{b,o}$	5.5	5.5	5.5	5.92
t_s	4.4	4.4	4.4	5.92

$$P = \frac{4K_\theta EI\theta}{L^2 cos(\theta)} \tag{6}$$

$$\sigma_{max} = \frac{Pac}{2I} \tag{7}$$

Following the analytical analysis of the unit cell, the dimensions of the reference design [20] are used to validate the models. The parameters are then adjusted for 3D printing (Sec. 2.7) and to account for the different variations in the main analysis. The dimensions of the samples are presented in Table 1, where both series and parallel configurations (Sec. 2.4) are provided for a single unit cell. Additionally, the dimensions for the different scaling variations are provided for the unit cell in a (2, 2) configuration, as the experiments uses the same (2, 2) sample for reference (Sec. 2.5). Each sample has an out of plane thickness of 8.25 mm, except in the case of uniform scaling, where this value is divided by n.

2.4 Series and Parallel. There are two ways to tessellate a square unit cell in the plane. First, in a *series configuration*, the unit cells are arranged along the y-direction. Each of the n cells is connected by linking the output of the previous unit cell to the C-shaped frame of the next, as shown in Fig. 4(*a*). In this setup, only the first unit cell is grounded, while only the last unit cell is actuated. Similar to a series of compression or extension springs, the internal force is uniform across all cells. The equivalent stiffness follows the series summation of the individual stiffnesses, so for identical unit cells, the overall stiffness is reduced by a factor of $1/n$. As the number of unit cells increases, the ROM grows proportionally, which also increases translational crosstalk between the x- and y-directions. The product of the DOF stiffness K_x and the ROM corresponds to the maximum actuation force, which remains constant: stiffness decreases by $1/n$, while the ROM increases by n.

Second, in a *parallel configuration*, the unit cells are tessellated along the x-direction, as shown in Fig. 4(*b*). Adjacent cells are connected by joining both their C-shaped frames and output links. The bottom of each unit cell is fixed to the ground, while the top is subjected to a common actuation force. This configuration behaves like parallel compression or extension springs, where the total stiffness is the sum of the individual stiffnesses. For shear cells, both stiffness and maximum force scale in the same manner. Thus, with m identical parallel unit cells, the total stiffness equals that of a single unit cell multiplied by m, assuming the connections do not alter unit cell behavior. Since all unit cells deform equally, the stress distribution is uniform, and the ROM of the parallel tessellation remains constant. Consequently, translational crosstalk between the x- and y-directions is also constant. Because unit cell rotation is assumed to be constrained, a sufficient number of parallel unit cells is required to eliminate rotation.

2.5 Scaling of Unit Cells. Two types of tessellations can be formed in the plane with a square unit cell: *square tessellations*,

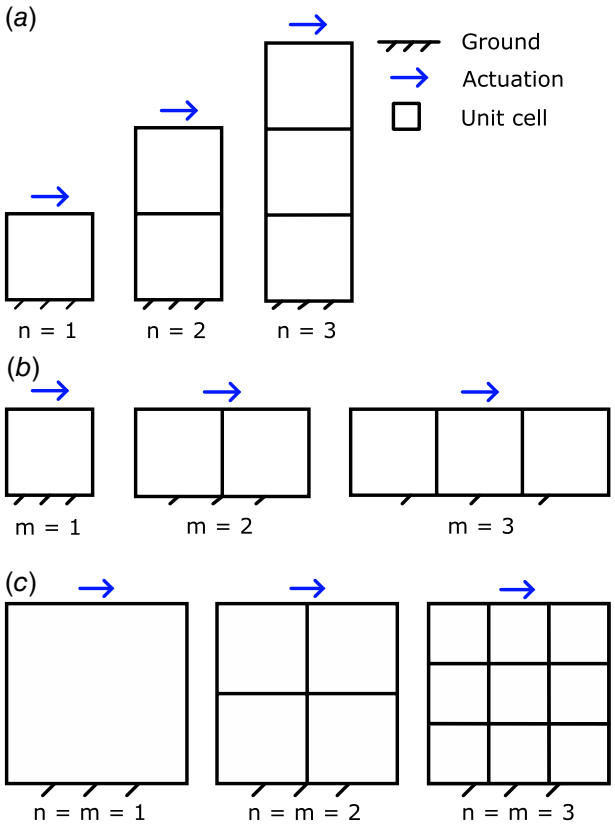

Fig. 4 Illustration of (*a*) series and (*b*) parallel tessellation, and (*c*) division scaling of unit cells

where $n = m$, and *rectangular tessellations*, where $n \neq m$. To study the effects of scaling and tessellation, three scaling approaches are considered. The first two are grouped under *division scaling*, illustrated in Fig. 4(*c*), where an initial area containing one unit cell is evenly divided into a square tessellation. The third, *scaling FT*, adapts rectangular tessellations of series and parallel arrangements by modifying the flexure thickness.

The *division scaling* approach has two variations. In *scaling AP*, all geometric parameters (length L, thickness t, and width w) are uniformly scaled by $1/n$. In *scaling LT*, only the length L and flexure thickness t are scaled by $1/n$, while the out-of-plane thickness remains constant. These variations differ in their effect on the DOF stiffness, as derived from Eq. (8). For *scaling LT*, stiffness remains constant because both L and t are cubed, and the numerator and denominator powers cancel. By contrast, *scaling AP* also reduces the width w, leading to a net stiffness reduction by $1/n$. For a square tessellation, the series and parallel effects cancel, so the stiffness of the unit cell and the tessellation are identical. Scaling does not affect the flexure stress, since L and t cancel in Eq. (9). However, the scaled unit cell produces smaller displacements, reduced by $1/n$ with respect to the original. This reduction is offset in the tessellation by the n cells in series, which restore the total range of motion. As a result, translational crosstalk also remains constant.

The third approach, *scaling FT*, adjusts the unit cell stiffness to maintain a constant overall DOF stiffness in both series and parallel tessellations. The DOF stiffness of a unit cell scales as

$$K_x \propto \frac{wt^3}{L^3} \tag{8}$$

where w is the width and L the flexure length. In a series tessellation, stiffness decreases by $1/n$, which can be compensated by increasing t by a factor of $\sqrt{[3]}n$. This adjustment, however, increases the unit cell stress σ_x, which is proportional to the flexure thickness

$$\sigma_x \propto \frac{t}{L} \tag{9}$$

leading to a reduced range of motion. Conversely, in a parallel tessellation, stiffness increases by a factor of m, which can be balanced by decreasing t by $\sqrt{[3]}1/m$. This lowers the stress in each flexure and increases the range of motion. Thus, *scaling FT* highlights the tradeoff between stiffness and range of motion: increasing one generally reduces the other.

2.6 Finite Element Method. For both simulation and experiment, the geometry is parametrically designed in SOLIDWORKS, allowing for tessellation and scaling. The geometry is saved as Parasolid (.X_T) files and imported into ANSYS WORKBENCH. The static structural module is used to simulate quasi-static load conditions, with large deflection enabled to account for geometric nonlinearities.

Polyethylene terephthalate glycol (PETG) is used as 3D printing material, which is well suited for compliant mechanisms due to its high toughness and moderate stiffness. The flexural modulus, or Young's modulus measured in bending [35], is $E = 2.1$ GPa, and Poisson's ratio is $\nu = 0.35$, with a yield stress of $\sigma_{\text{yield}} = 51$ MPa.

To control the mesh size, ANSYS's standard meshing resolution is used for the rigid bodies, as they experience only small deformations and low stress. In contrast, the flexures undergo highly concentrated deformations and therefore require mesh refinement. A convergence study showed that the flexures converge with face sizing set to an element size of the flexure length divided by 24. Figure 5(*a*) shows the resulting mesh, highlighting the contrast between the fine mesh at the flexures and the coarse mesh at the rigid bodies. The element type selected by ANSYS is SOLID187, a quadratic element well suited for irregular meshes and large deformations.

The boundary conditions are illustrated in Fig. 5(*b*) for a (3, 3) tessellation. To simulate the sample, the base link is fixed using a fixed surface constraint, shown at the top of the mechanism. To actuate the output link, a displacement is applied to the on the output link at bottom of the mechanism in Fig. 5(*b*). For the stiffness calculation a deformation of 0.1 mm is applied, while stress and crosstalk are measured at the calculated ROM. Probing the deformation at the actuated surface verifies that the applied displacement is reached, and the probed reaction force is used in combination with this deformation to calculate the stiffness. To measure the crosstalk two displacement probes are used at the sides of the output link. The translational and rotational crosstalk can be computed by taking the average or dividing the difference by the length of the link.

Figure 5(*c*) shows the deformation and stress of a (3, 3) configuration. As expected, the locations of the highest stress correspond with the joint locations in the PRBM. In the square configurations for scaling the unit cells, the number of elements increases rapidly, therefore the scaling simulations are carried out on the unit cells with the output link constrained in rotation and the (n, n) unit cells for n equal to 2, 4 and 6 and are illustrated in Fig. 6.

2.7 Experiment. The samples were 3D printed using a BambuLab X1C printer with PETG material. For the parallel, series, and series with scaling FT configurations, a 0.4 mm nozzle was used with three walls and 25% gyroid infill. The gyroid pattern was selected for its near-isotropic behavior, attributed to its circular mesh structure. For the parallel with scaling FT and the scaling AP and LT variations, a 0.2 mm nozzle was employed, as the flexures are thinner in these cases. These samples were printed with four walls and the same 25% gyroid infill. Special care was taken to avoid seams on thin flexures to prevent weak spots that could act

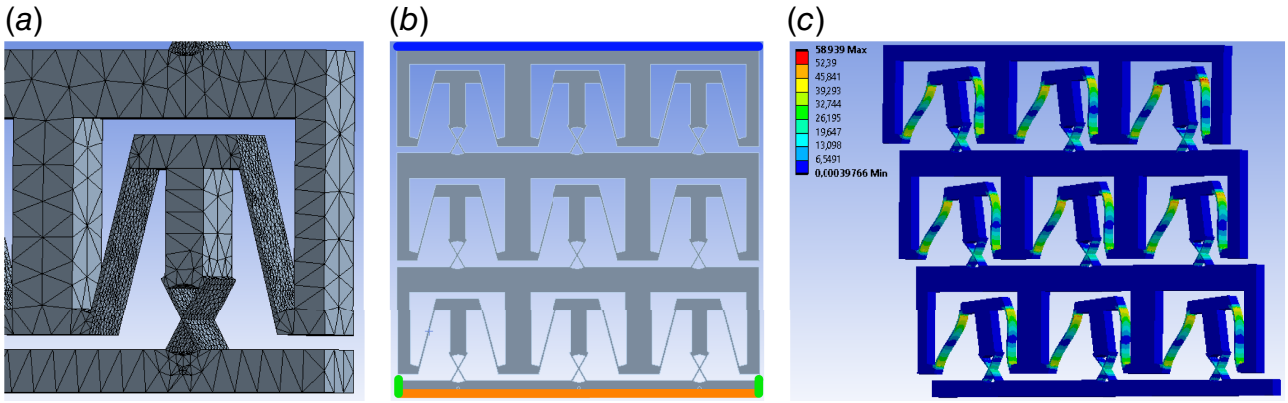

Fig. 5 Illustration of the FEM setup with (*a*) the mesh with face sizing at the flexures, (*b*) the boundary conditions with the fixed base at the top of the mechanism, the actuation displacement at the bottom, and the measured displacement locations on the extremities of the actuated mechanism, and (c) the typical deformation and stress

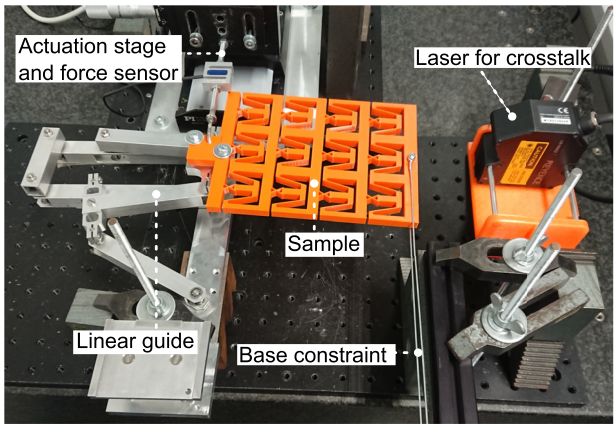

Fig. 6 Photograph of the experimental setup, showing the key components

as notched joints. Each variation was tested using tessellations with m and n equal to 2, 4, and 6.

The experimental setup, shown in Fig. 6, was designed to characterize stiffness and crosstalk (both translational and rotational). A PI motion stage was used for actuation, with a Futek LSB200-FSH0387 force sensor mounted at its output. The system was operated using a custom LABVIEW program tailored for actuator–sensor integration. Experiments were repeated five times for each configuration to obtain averaged results. The first measurement of each set was discarded to mitigate conditioning effects in the PETG material, which can cause pronounced hysteresis in initial runs.

The Roberts mechanism expands perpendicular to the primary direction of motion. Fixing the base link introduces an off-axis force on the force sensor. To minimize this effect, the output link was clamped onto a low-friction linear guide mechanism, which combines the Roberts mechanism with a parallelogram linkage. During testing, the actuation stage was displaced through the sample's range of motion while the corresponding force–displacement curve was recorded. Data were imported into PYTHON, where the five test runs were processed, and two points were selected to calculate stiffness by dividing the change in force by the change in displacement. Visual inspection verified that the resulting stiffness curves aligned with the expected slope.

Crosstalk occurs at the base link of the sample, which was constrained using two slender iron wires and bolts. This arrangement approximates a prismatic–revolute joint, allowing both translational and rotational crosstalk. A Keyence LK-H052 laser displacement sensor was positioned at the center of the base link, and 50 mm offset to the left, to measure crosstalk. Crosstalk was measured manually and recorded in Excel. Translational crosstalk was determined from the center displacement, while rotational crosstalk was obtained by dividing the difference between the left and center displacements by their 50 mm separation.

3 Results: Influence of Tessellation and Scaling

In this section, we analyze the influence of tessellating the Roberts shear cell (with dimensions listed in Table 1) in both series and parallel configurations. The effects of scaling on ROM, stiffness, and crosstalk are examined, and the analytical model is validated against FEM and experimental results. The series analysis, experiments, and simulations were performed with $m = 3$ to constrain rotation.

Figure 7(*a*) shows the evolution of the ROM, calculated using the analytical model, for series tessellations (3, n) and parallel tessellations (m, 1), with unit cell counts ranging from 1 to 10. The evolution of the *scaling FT* approach is also presented, with a scaling factor of $\sqrt{[3]}n$ for the series configuration and $\sqrt{[3]}1/m$ for the parallel configuration. In the series case, the ROM increases linearly with n. Applying *scaling FT* reduces the ROM relative to the unscaled tessellation. By contrast, the parallel tessellation maintains a constant ROM as m increases, while applying *scaling FT* increases the ROM. Both *division scaling* variations (AP and LT) preserve the expected constant ROM. The unit cell (UC) ROM follows the expected $1/n$ trend relative to cell size.

Figure 7(*b*) presents the evolution of stiffness K_x for the parallel tessellation (m, 1) compared with the parallel *scaling FT* case. As expected, stiffness increases linearly with m. In the *scaling FT* case, however, the reduction in unit cell stiffness offsets the additional cells, yielding an overall constant stiffness. In both cases, FEM results align closely with the analytical model. Experimental results follow the same general trend but show higher stiffness values for parallel samples, which will be discussed further in Sec. 4.

Figure 7(*c*) shows the evolution of stiffness K_x for the series tessellation (3, n) compared with the series *scaling FT* tessellation and a single UC. As predicted, the stiffness of the series tessellation decreases proportionally to $1/n$. In contrast, the series with *scaling FT* maintains a constant stiffness, while the unit cell stiffness increases linearly with n. FEM and experimental results for the series tessellation closely match the analytical predictions.

Figure 7(*d*) presents the stiffness K_x for square tessellations ($n = m$) and the isolated UC under *scaling AP*, where all parameters are scaled, and *scaling LT*, where only the flexure length and thickness are scaled. The *scaling AP* case follows the expected $1/n$ trend, though FEM and experimental results show a small offset. The *scaling LT* case maintains constant stiffness, with analytical and

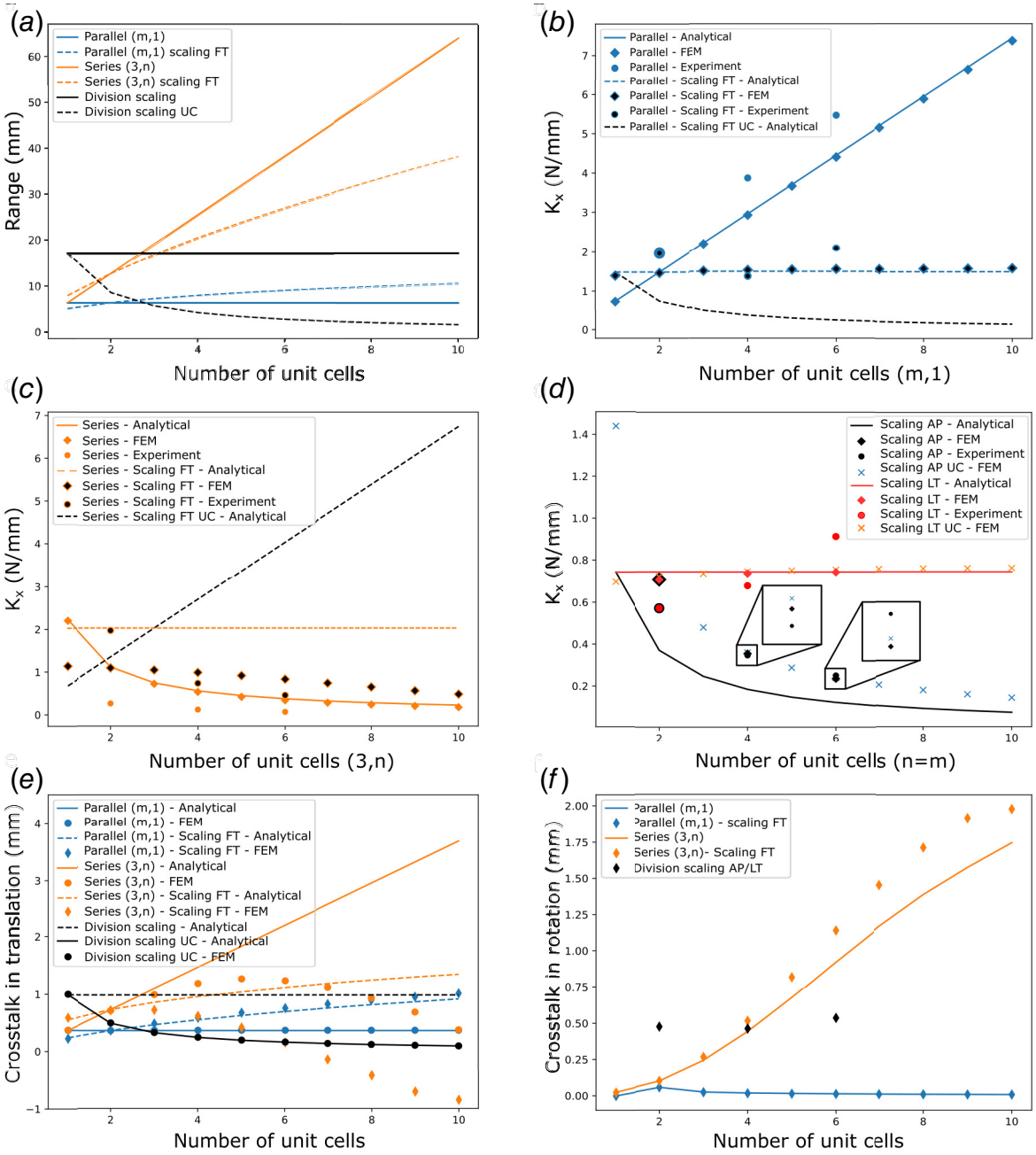

Fig. 7 Evolution of (*a*) the calculated range of motion, (*b*) the stiffness K_x for parallel tessellation, (*c*) the stiffness K_x for series tessellation, (*d*) the stiffness K_x for division scaling, (*e*) the FEM and analytical translational crosstalk, and (*f*) the FEM rotational crosstalk

FEM results in close agreement. Experimental results, however, show an increasing trend for small n. Both approaches confirm that the unit cell and the $n = m$ tessellations yield equivalent results.

Figure 7(*e*) illustrates the evolution of translational crosstalk, computed with FEM and the analytical model, for parallel (m, 1) and series (3, n) tessellations, including the *scaling FT* and *division scaling* cases. As expected, the parallel tessellation and both *division scaling* variations exhibit constant crosstalk, consistent with their constant RoM. The parallel *scaling FT* case shows an increase in crosstalk. For the series tessellation, the analytical model predicts a linear increase, whereas FEM results decrease beyond $n = 4$. The series *scaling FT* case follows a similar pattern, with FEM diverging from the analytical prediction as n increases. This discrepancy becomes more pronounced with larger n and is examined in Sec. 4.

The evolution of the rotational crosstalk (around the z-axis) is shown in Fig. 7(*f*) for parallel (m, 1), series (3, n), their *scaling FT*, and the *division scaling* with $n = m$. The results for the series tessellations indicate that rotational crosstalk increases significantly with the number of unit cells. In contrast, for the parallel tessellation, rotational crosstalk decreases as m increases and remains close to zero. For $m = 1$ and for the unit cell in division scaling, the rotation is constrained in simulation, resulting in zero crosstalk. However, for the overall structure in division scaling, the rotation remains approximately constant.

4 Discussion

The results generally align well with analytical predictions and FEM simulations, validating key assumptions about stiffness

and ROM in metamaterial motion systems. These findings provide a foundation for tuning metamaterial performance through tessellation and scaling choices. In a rectangular tessellation, where $m \neq n$ it is possible to tune the stiffness, range of motion, and crosstalk with the number of unit cells. The results show that scaling the unit cells using *division scaling* ($n = m$) does not alter the overall behavior of the metamaterial mechanism. In contrast, scaling only the flexure thickness (*scaling FT*) enables fine-tuning of the behavior. In this study, a single scaling factor that increases with the number of unit cells is applied. However, alternative scaling strategies could be used to target specific parameters or performance characteristics.

Despite overall agreement, some deviations between the model and both experimental and FEM results emerge, primarily due to large deformation effects, particularly in series configurations. Increased rotation in these arrangements affects both stiffness and crosstalk, likely due to the rotational degrees-of-freedom in the unit cells. More constrained unit cell designs or the addition of parallel unit cells may help mitigate these effects. Parallel configurations generally align with predictions, though experimental stiffness values are slightly higher than expected. While 3D printing enabled cost-effective production of multiple sample variations, surface imperfections in parallel unit cells increased the effective flexure thickness. Experimental crosstalk results were inconsistent, potentially due to finite frame stiffness, polymer creep, or sensor temperature variations. Consequently, the experimental crosstalk data did not provide sufficient additional insight to justify separate graphical representations.

The findings are not limited to the specific shear unit cell examined. A simple spring analogy allows for generalization to other unit cell types, such as linear unit cells, following similar stiffness derivations. The stiffness of an (m, n) tessellation can be determined by combining the series and parallel approximations. These results provide designers with a fast and effective way to estimate the behavior of metamaterial motion systems, enabling rapid iteration and the exploration of more complex unit cell designs. The ability to make quick yet accurate estimations is valuable for both conceptual studies and refining designs for practical applications.

The planar straight-line metamaterial mechanism proposed in this study could be further investigated with respect to the in-plane constraint stiffness (K_y) and out-of-plane stiffness (K_z), where similar derivations could be applied. A tessellation of straight-line metamaterial mechanism can serve as a building block for more complex planar systems. For instance, a (4, 4) tessellation was mirrored in an alternative design as an attempt to compensate crosstalk (Fig. 8(*a*)). However, this approach proved ineffective. In contrast, an opposing system (Fig. 8(*b*)), where the two sides are constrained, successfully suppresses crosstalk and exhibits a slight increase in stiffness.

In addition, the planar mechanism can serve as a building block for spatial straight-line metamaterial mechanisms. For instance, an orthogonal configuration (Fig. 8(*c*)), reduces the need for out of plane stiffness. The orthogonal and opposing behaviors can be combined into a general revolved configuration (Fig. 8(*d*)), where N planar mechanisms are arranged around the motion axis. Lastly, a planar series configuration can be used to obtain a 2DOF metamaterial mechanism (Fig. 8(*e*)).

These findings open several avenues for future research and applications of metamaterial mechanisms. Understanding the tradeoffs between stiffness and range of motion enables the integration of sensing and actuation elements, supporting distributed sensing and actuation strategies. Future work could explore 3D configurations to overcome stiffness limitations, incorporate tunable stiffness mechanisms, and design highly precise compliant motion stages. The ability to control mechanical properties at the unit cell level extends the relevance of these results beyond motion systems to applications such as multistable mechanisms,

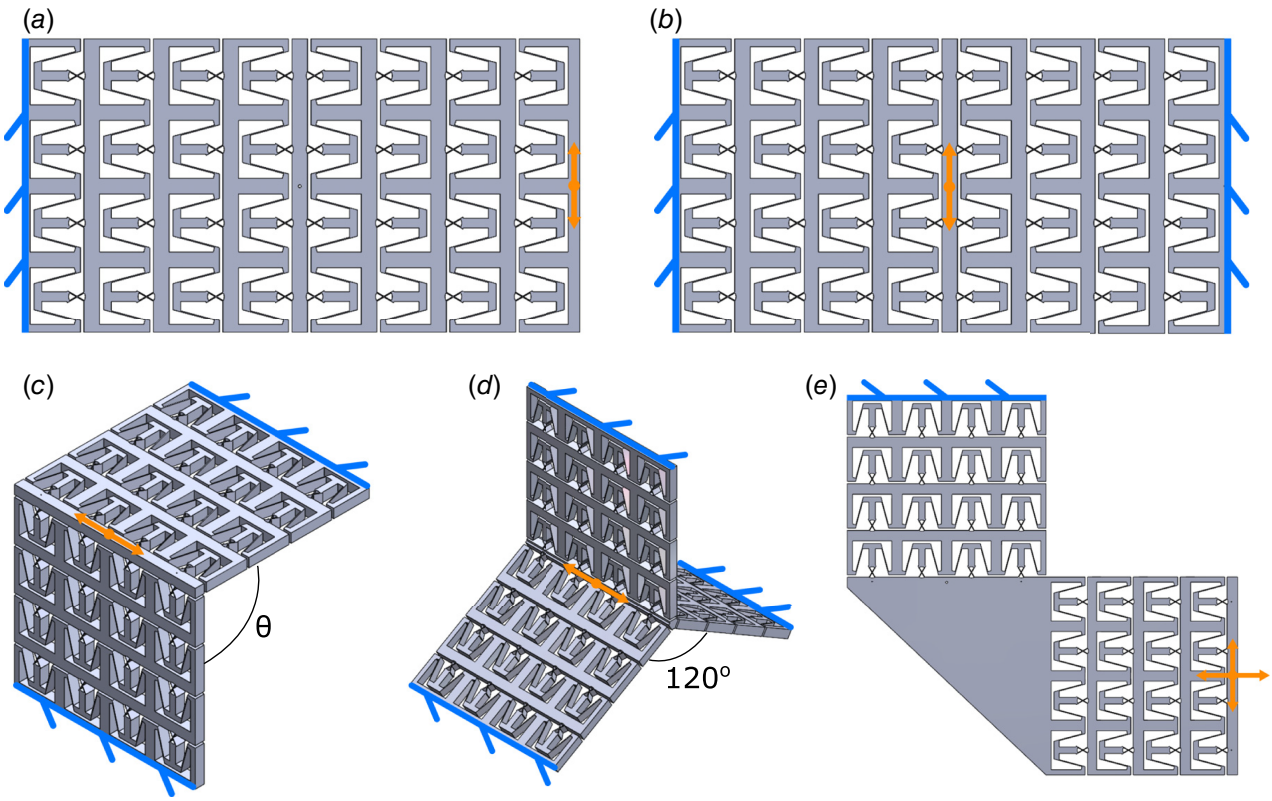

Fig. 8 Representation of the use of the planar shear metamaterial mechanism as building blocks for spatial metamaterials in (*c*) alternating, (*b*) opposing, (*c*) orthogonal, and (*d*) revolved configurations, and (*e*) a series configuration to obtain a 2DOF metamaterial, with the fixed connections and directions of motion

soft robotics, and MEMS-based compliant structures. By applying the principles established in this study, designers can optimize metamaterial motion systems for greater mechanical efficiency, enhanced functionality, and improved adaptability in advanced engineering applications.

5 Conclusion

We presented a design for straight-line metamaterial mechanisms based on an approximate shear cell embodiment. The approach involves utilizing a straight-line mechanism as shear cells and tessellating the cell to create metamaterial mechanisms. The Roberts mechanism was selected as a shear cell due to its compactness and simplicity, despite exhibiting some parasitic motion.

Compared to a single unit cell, series tessellation significantly increases the range of motion while reducing stiffness and increasing crosstalk. In contrast, parallel tessellation increases stiffness while maintaining a constant range of motion and reducing crosstalk. Additionally, the study on division scaling demonstrated that arranging the metamaterial surface in a square lattice ($m = n$) does not alter the range of motion or crosstalk. In addition, the stiffness remains unchanged when the length and thickness of the flexures are modified under the applied scaling. The tessellation of the Roberts cell in a rectangular lattice ($n \neq m$) provides the potential for tuning the range of motion, stiffness, and crosstalk.

Overall, these findings provide a valuable contribution to the field of straight-line metamaterial mechanisms and can serve as a basis for the analysis and design of linear guiding systems and applied metamaterials.

Acknowledgment

This publication is part of the project Mechanical Metamaterials for Compact Motion Systems (MECOMOS), project no. 18940 of the Open Technology Program financed by the Dutch Research Council (NWO).

Data Availability Statement

The authors attest that all data for this study are included in the article.

Appendix: Extended Equations

This appendix provides detailed derivations of the PRBM, vector loop solutions, actuation force, and flexure stress, supplementing the main text (Eqs. (1)–(7)). The unknowns of the vector loop equations (Eqs. (1) and (2) in the main text) are the joint angles θ_3, θ_4, θ_6, and the output link length L_6. Each vector $\vec{r_i}$ is expressed in terms of its real and imaginary parts, allowing the loop equations to be solved algebraically. In particular, θ_4 is obtained using the tangent half-angle formula (Eq. (A2)), with the remaining unknowns calculated as given in Eqs. (A1)–(A4). The resulting output vector can be decomposed into x and y components (Eqs. (A5) and (A6))

$$\theta_3 = \cos^{-1}\left(\frac{L_4\cos(\theta_4) - L_2\cos(\theta_2) + L_1}{L_3}\right) \tag{A1}$$

$$\theta_4 = 2\tan^{-1}(t) \tag{A2}$$

$$\theta_6 = \tan^{-1}\left(\frac{L_2\sin(\theta_2) + \frac{1}{2}L_3\sin(\theta_3) - L_5\sin(\theta_3 + 90\,\text{deg})}{L_2\cos(\theta_2) + \frac{1}{2}L_3\cos(\theta_3) - L_5\cos(\theta_3 + 90\,\text{deg})}\right) \tag{A3}$$

$$L_6 = \frac{L_2\cos(\theta_2) + \frac{1}{2}L_3\cos(\theta_3) - L_5\cos(\theta_3 + 90\,\text{deg})}{\cos(\theta_6)} \tag{A4}$$

$$x = L_6\cos(\theta_6) \tag{A5}$$

$$y = L_6\sin(\theta_6) \tag{A6}$$

The actuation force is derived using the principle of virtual work [33], where the external virtual work equals the internal potential energy of the torsional springs, given in Eq. (A7). Here, ϕ_i is the relative angle between links, and $\delta\phi_i$ denotes its virtual rotation. For joint 2, these relations are given in Eqs. (A8) and (A9). The displacement of the actuation force is determined by summing the x-components of vectors 2, 3, and 5 (Eq. (A10)), with the corresponding virtual displacement given in Eq. (A11). Substituting these expressions into Eq. (A7) and solving for F yields Eq. (A12). Rewriting for solvability leads to Eq. (5), with substitutions A–E defined in Eqs. (A13)–(A17). From the expression in Eq. (5), the relations between $\delta\theta_i$ can be substituted using Freudenstein's kinematic coefficients; the detailed derivation is omitted here.

$$F\,\delta x = \sum_i K_i\phi_i\delta\phi_i \tag{A7}$$

$$\phi_2 = (\theta_2 - \theta_{20}) - (\theta_3 - \theta_{30}) \tag{A8}$$

$$\delta\phi_2 = \delta\theta_2 - \delta\theta_3 \tag{A9}$$

$$x = L_2\cos(\theta_2) + \frac{L_3}{2}\cos(\theta_3) + L_5\sin(\theta_3) \tag{A10}$$

$$\delta x = -L_2\sin(\theta_2)\delta\theta_2 + \left(-\frac{L_3}{2}\sin(\theta_3) + L_5\cos(\theta_3)\right)\delta\theta_3 \tag{A11}$$

$$F = \frac{(K_1\phi_1 + K_2\phi_2)\,\delta\theta_2 + (K_3\phi_3 + K_5\phi_3 - K_2\phi_2)\,\delta\theta_3}{-L_2\sin(\theta_2)\,\delta\theta_2 + \left(-\frac{L_3}{2}\sin(\theta_3) + L_5\cos(\theta_3)\right)\delta\theta_3} + \frac{(K_4\phi_4 - K_3\phi_3)\,\delta\theta_4}{-L_2\sin(\theta_2)\,\delta\theta_2 + \left(-\frac{L_3}{2}\sin(\theta_3) + L_5\cos(\theta_3)\right)\delta\theta_3} \tag{A12}$$

$$A = K_1\phi_1 + K_2\phi_2 \tag{A13}$$

$$B = K_3\phi_3 - K_2\phi_2 + K_5\phi_5 \tag{A14}$$

$$C = K_4\phi_4 - K_3\phi_3 \tag{A15}$$

$$D = -L_2\sin(\theta_2) \tag{A16}$$

$$E = -\frac{L_3}{2}\sin(\theta_3) + L_5\cos(\theta_3) \tag{A17}$$

In the stress derivation (Eq. (7)), a is the orthogonal distance between the base of the flexure and the equivalent force P (Eq. (6)). This distance depends on the characteristic radius factor γ, link length, and relevant joint angles. For the leaf spring of link 2, the expression for a is

$$a = \frac{1-\gamma}{2}L_2 + \gamma L_2\cos(\theta_2 - \theta_{2,0}) + \frac{1-\gamma}{2}L_2\cos(\theta_3 - \theta_{3,0}) \tag{A18}$$

References

[1] Wang, Z., Luan, C., Liao, G., Liu, J., Yao, X., and Fu, J., 2020, "Progress in Auxetic Mechanical Metamaterials: Structures, Characteristics, Manufacturing Methods, and Applications," Adv. Eng. Mater., **22**(10), p. 2000312.

[2] Liu, J., and Zhang, Y., 2018, "Soft Network Materials With Isotropic Negative Poisson's Ratios Over Large Strains," Soft Matter, **14**(5), pp. 693–703.

[3] Li, Q., Yang, D., and Mao, X., 2022, "Pressure-Resistant Cylindrical Shell Structures Comprising Graded Hybrid Zero Poisson's Ratio Metamaterials With Designated Band Gap Characteristics," Marine Struct., **84**, p. 103221.

[4] Alderson, A., and Alderson, K. L., 2007, "Auxetic Materials," Proc. Inst. Mech. Eng., Part G: J. Aeros. Eng., **221**(4), pp. 565–575.

[5] Mueller, J., Lewis, J. A., and Bertoldi, K., 2022, "Architected Multimaterial Lattices With Thermally Programmable Mechanical Response," Adv. Funct. Mater., **32**(1), p. 2105128.

[6] Findeisen, C., Hohe, J., Kadic, M., and Gumbsch, P., 2017, "Characteristics of Mechanical Metamaterials Based on Buckling Elements," J. Mech. Phys. Solids, **102**, pp. 151–164.

[7] Yang, H., and Ma, L., 2020, "1D to 3D Multi-Stable Architected Materials With Zero Poisson's Ratio and Controllable Thermal Expansion," Mater. Des., **188**, p. 108430.

[8] Zou, B., Liang, Z., Zhong, D., Cui, Z., Xiao, K., Shao, S., and Ju, J., 2023, "Magneto-Thermomechanically Reprogrammable Mechanical Metamaterials," Adv. Mater., **35**(8), p. 2207349.

[9] Ion, A., Frohnhofen, J., Wall, L., Kovacs, R., Alistar, M., Lindsay, J., Lopes, P., Chen, H.-T., and Baudisch, P., 2016, "Metamaterial Mechanisms," Proceedings of the 29th Annual ACM Symposium on User Interface Software and Technology (UIST '16), Tokyo, Japan, Oct. 16–19, pp. 529–539.

[10] Li, J., Yang, Q., Huang, N., and Tao, R., 2021, "A Novel Mechanical Metamaterial With Tailorable Poisson's Ratio and Thermal Expansion Based on a Chiral Torsion Unit," Smart Mater. Struct., **30**(11), p. 115004.

[11] Frenzel, T., Hahn, V., Ziemke, P., Schneider, J. L. G., Chen, Y., Kiefer, P., Gumbsch, P., and Wegener, M., 2021, "Large Characteristic Lengths in 3D Chiral Elastic Metamaterials," Commun. Mater., **2**(1), pp. 1–9.

[12] Roberjot, P., and Herder, J. L., 2024, "A Unified Design Method for 2D Auxetic Metamaterials Based on a Minimal Auxetic Structure," Int. J. Solids Struct., **295**, p. 112777.

[13] Grima, J. N., Attard, D., Caruana-Gauci, R., and Gatt, R., 2011, "Negative Linear Compressibility of Hexagonal Honeycombs and Related Systems," Scr. Mater., **65**(7), pp. 565–568.

[14] Zhao, H., Bi, S., and Yu, J., 2012, "A Novel Compliant Linear-Motion Mechanism Based on Parasitic Motion Compensation," Mech. Mach. Theory, **50**, pp. 15–28.

[15] Buckley, J., and Huang, M. Z., 2012, "A Study on Dimension Synthesis for the Peaucellier Mechanism," Proceedings of the ASME 2012 International Design Engineering Technical Conferences and Computers and Information in Engineering Conference (IDETC/CIE 2012), Chicago, IL, Aug. 12–15, pp. 233–239.

[16] Hricko, J., 2014, "Design of Compliant Micro-Stage Based on Peaucellier-Lipkin Straight-Line Mechanism," 2014 23rd International Conference on Robotics in Alpe-Adria-Danube Region (RAAD), Smolenice, Slovakia, Sept. 3–5, pp. 1–6.

[17] Huang, M. Z., 2019, "On Dimension Synthesis of Hart's Inversor III Straight-Line Mechanism as a Precision Robotic End-of-Arm Tool," American Society of Mechanical Engineers Digital Collection.

[18] Singh, S., and Chaudhary, R., 2020, "Analysis of Watt's Linkage Under Dynamic Loading," Mater. Today: Proc., **27**(Part 2), pp. 963–967.

[19] Pei, X., Yu, J., Zong, G., and Bi, S., 2014, "Design of Compliant Straight-Line Mechanisms Using Flexural Joints," Chin. J. Mech. Eng., **27**(1), pp. 146–153.

[20] Wan, S., and Xu, Q., 2016, "Design and Analysis of a New Compliant XY Micropositioning Stage Based on Roberts Mechanism," Mech. Mach. Theory, **94**, pp. 1–13.

[21] Pavlović, N. T., and Pavlović, N. D., 2009, "Compliant Mechanism Design for Realizing of Axial Link Translation," Mech. Mach. Theory, **44**(5), pp. 1082–1091.

[22] Sheffield, J. L., Sargent, B., and Howell, L. L., 2023, "Embedded Linear-Motion Developable Mechanisms on Cylindrical Surfaces," ASME J. Mech. Rob., **16**(1), p. 015001.

[23] Qian, W., Yang, Y., Qu, Z., Jin, Z., and Guo, R., 2024, "Synthesis and Robust Design of Approximate Straight-Line Mechanism With Instantaneous Center at Infinity," J. Brazil. Soc. Mech. Sci. Eng., **46**(5), pp. 1–13.

[24] Zhang, Y., Wang, Q., Tichem, M., and van Keulen, F., 2020, "Design and Characterization of Multi-Stable Mechanical Metastructures With Level and Tilted Stable Configurations," Extreme Mech. Lett., **30**, p. 100593.

[25] McCarthy, B., Nail, E., Nagarajan, A., McCullough, J., and Hopkins, J. B., 2023, "Design of Configuration Indifferent Compliant Building Blocks," Precis. Eng., **81**, pp. 60–67.

[26] Hao, G., Li, H., He, X., and Kong, X., 2014, "Conceptual Design of Compliant Translational Joints for High-Precision Applications," Front. Mech. Eng., **9**(4), pp. 331–343.

[27] Shaw, L. A., Chizari, S., Dotson, M., Song, Y., and Hopkins, J. B., 2018, "Compliant Rolling-Contact Architected Materials for Shape Reconfigurability," Nat. Commun., **9**(1), p. 4594.

[28] Hongzhe, Z., Shusheng, B., Jingjun, Y., and Jun, G., 2012, "Design of a Family of Ultra-Precision Linear Motion Mechanisms," ASME J. Mech. Rob., **4**(4), p. 041012.

[29] Yang, Y., Zhang, X., Maiolino, P., Chen, Y., and You, Z., 2023, "Linkage-Based Three-Dimensional Kinematic Metamaterials With Programmable Constant Poisson's Ratio," Mater. Des., **233**, p. 112249.

[30] Gu, Y., Zhang, X., Wei, G., and Chen, Y., 2024, "Sarrus-Inspired Deployable Polyhedral Mechanisms," Mech. Mach. Theory, **193**, p. 105564.

[31] Li, Z., Schicho, J., and Schröcker, H.-P., 2015, "Spatial Straight-Line Linkages by Factorization of Motion Polynomials," ASME J. Mech. Rob., **8**(1), p. 021002.

[32] Farhadi Machekposhti, D., Tolou, N., and Herder, J. L., 2015, "A Review on Compliant Joints and Rigid-Body Constant Velocity Universal Joints Toward the Design of Compliant Homokinetic Couplings," ASME J. Mech. Des., **137**(3), p. 032301.

[33] Howell, L., 2001, *Compliant Mechanisms, A Wiley-Interscience Publication*, Wiley.

[34] Howell, L. L., Magleby, S. P. , and Olsen, Brian M., 2013, *Handbook of Compliant Mechanisms*, John Wiley & Sons, Ltd.

[35] Mujika, F., Carbajal, N., Arrese, A., and Mondragon, I., 2006, "Determination of Tensile and Compressive Moduli by Flexural Tests," Polym. Test., **25**(6), pp. 766–771.